Inorganic Chemistry

Article

pubs.acs.org/IC

Synthesis and Characterization of Nitrogen-Rich Macrocyclic Ligands and an Investigation of Their Coordination Chemistry with Lanthanum(III)

Justin J. Wilson,* Eva R. Birnbaum,* Enrique R. Batista, Richard L. Martin, and Kevin D. John

Los Alamos National Laboratory, P.O. Box 1663, Los Alamos, New Mexico 87545, United States

Supporting Information

ABSTRACT: Derivatives of the ligand 1,4,7,10-tetraazacyclododecane (cyclen) containing pendant N-heterocyclic donors were prepared. The heterocycles pyridine, pyridazine, pyrimidine, and pyrazine were conjugated to cyclen to give 1,4,7,10-tetrakis(pyridin-2-ylmethyl)-1,4,7,10-tetraazacyclododecane (L^{py}), 1,4,7,10-tetrakis(3-pyridazylmethyl)-1,4,7,10-tetraazacyclododecane (L^{pyd}), 1,4,7,10-tetrakis(4-pyrimidylmethyl)-1,4,7,10-tetraazacyclododecane (L^{pyr}), and 1,4,7,10-tetrakis(2-pyrazinylmethyl)-1,4,7,10-tetraazacyclododecane (L^{pz}), respectively. The coordination chemistry of these ligands was explored using the La^{3+} ion. Accordingly, complexes of the general formula $[La(L)(OTf)](OTf)_2$, where OTf = trifluoromethanesulfonate and L = L^{py} (**1**), L^{pyd} (**2**), L^{pyr} (**3**), and L^{pz} (**4**), were synthesized and characterized by NMR spectroscopy. Crystal structures of **1** and **2** were also determined by X-ray diffraction studies, which revealed 9-coordinate capped, twisted square-antiprismatic coordination geometries for the central La^{3+} ion. The conformational dynamics of **1**−**4** in solution were investigated by variable-temperature NMR spectroscopy. Dynamic line-shape and Eyring analyses enabled the determination of the activation parameters for the interconversion of enantiomeric forms of the complexes. Unexpectedly, the different pendant N-heterocycles of **1**−**4** give rise to varying values for the enthalpies and entropies of activation for this process. Density functional theory calculations were carried out to investigate the mechanism of this enantiomeric interconversion. Computed activation parameters were consistent with those experimentally determined for **1** but differed somewhat from those of **2**−**4**.

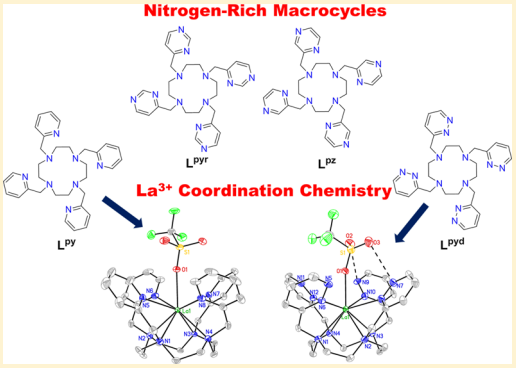

INTRODUCTION

The unique physical properties of lanthanide ions render them useful for a number of biological applications. Complexes of these ions are used as luminescent sensors, MRI contrast agents, and radionuclide therapy and imaging agents.[1−6] To fully maximize their potential, the design of ligands that are capable of stabilizing these labile and easily hydrolyzable ions in aqueous solution is necessary. Because lanthanides preferably attain high coordination numbers, ligand design has focused on multidentate ligands with an emphasis placed on those with eight or more donor atoms.

A promising class of ligands are those based on 1,4,7,10-tetraazacyclododecane-1,4,7,10-tetraacetic acid (DOTA) (Chart 1).[7] DOTA contains a macrocyclic cyclen base with four pendant carboxylate groups. The resulting anionic, octadentate lanthanide complexes of DOTA are incredibly stable. The success of DOTA has motivated the synthesis of a wide range of analogues. Among these is the ligand 1,4,7,10-tetrakis(pyridin-2-ylmethyl)-1,4,7,10-tetraazacyclododecane (L^{py}) (Chart 1), where the pendant carboxylates are replaced with pyridines. This ligand was first prepared to model the active sites of metalloenzymes and -proteins[8−11] and has subsequently been used to form anticancer and antiviral Bi^{3+} complexes[12−14] and to selectively extract Na^+ in the presence of competing alkali metal ions.[15] Only recently has the lanthanide coordination chemistry of L^{py} been explored for luminescence-sensitization applications.[16−18]

In this Article, new derivatives of L^{py} in which the pyridine is replaced with pyridazine (L^{pyd}), pyrimidine (L^{pyr}), and pyrazine (L^{pz}) are reported (Chart 1). Both the addition and location of the additional nitrogen atoms in these newly prepared analogues affect both their relative donor strength and chemical hardness. The coordination chemistry of these ligands with the La^{3+} ion was explored. The interconversion of the La^{3+} complexes from twisted square-antiprismatic geometries (TSAP) to square-antiprismatic (SAP) geometries was probed by variable-temperature NMR spectroscopy. Unexpectedly, the activation parameters for this interconversion process were found to depend strongly on the ligand employed. Computational studies investigating the mechanism of this interconversion process are also presented.

RESULTS AND DISCUSSION

Ligand Synthesis and Characterization. Synthesis of L^{py} was carried out as previously reported by the reaction of slightly

Received: July 29, 2014
Published: December 19, 2014

   dx.doi.org/10.1021/ic501843c | Inorg. Chem. 2015, 54, 97−109

Chart 1. Structures and Abbreviated Names of the Ligands Discussed and Investigated in This Article

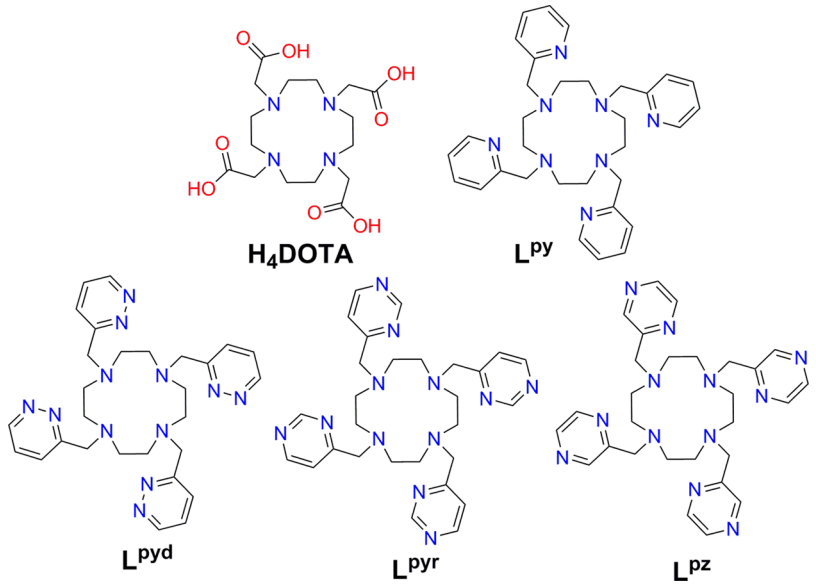

Scheme 1. Synthesis of Ligands Described in This Article[a]

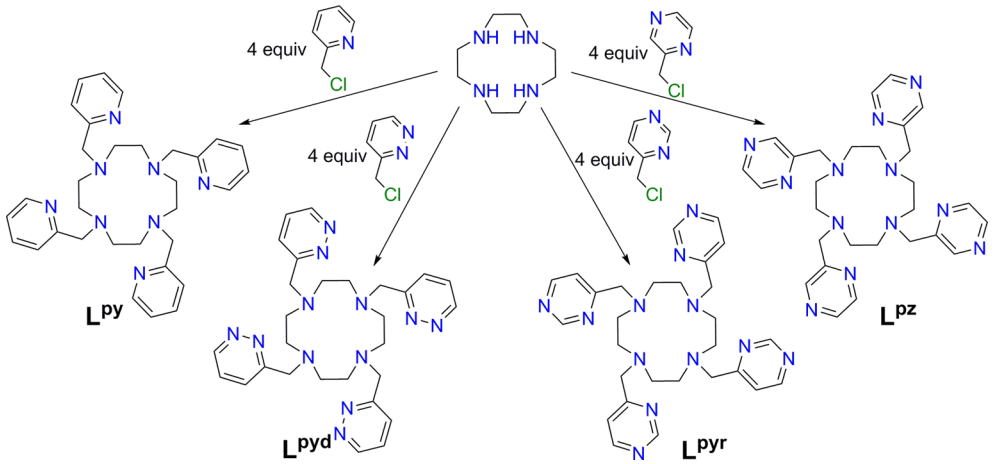

[a]Reaction conditions: refluxing CH_3CN and 20 equiv of Cs_2CO_3.

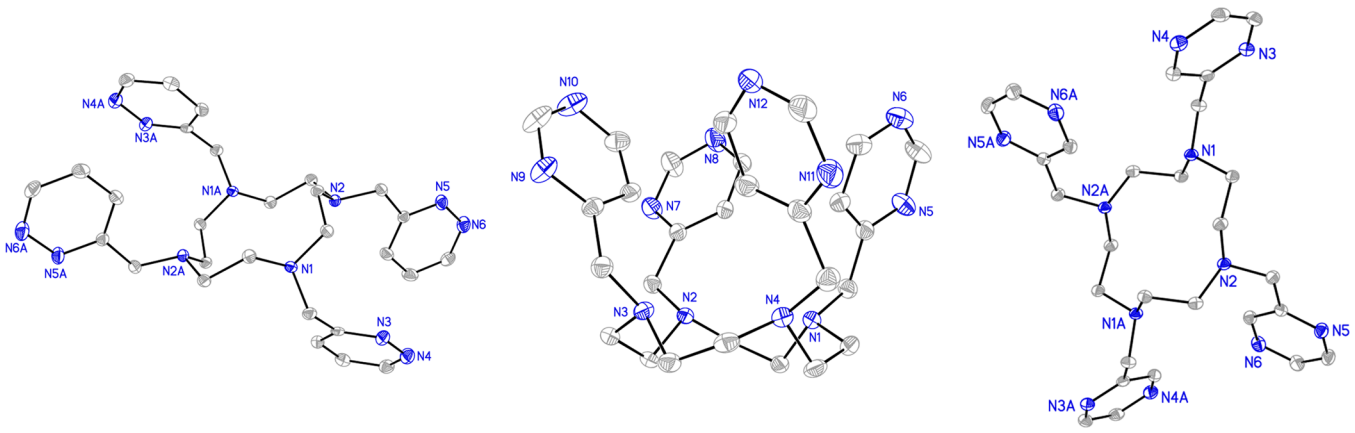

Figure 1. X-ray crystal structures of L^{pyd} (left), L^{pyr} (center), and L^{pz} (right). Hydrogen atoms have been omitted for clarity. Ellipsoids are drawn at 50% probability levels.

greater than 4 equiv of commercially available 2-picolyl chloride with 1,4,7,10-tetraazacyclododecane (cyclen) in the presence of excess Cs_2CO_3 in CH_3CN.[18] For the newly reported ligands L^{pyd}, L^{pyr}, and L^{pz}, the corresponding chloromethyl N-heterocycles,

dx.doi.org/10.1021/ic501843c | Inorg. Chem. 2015, 54, 97−109

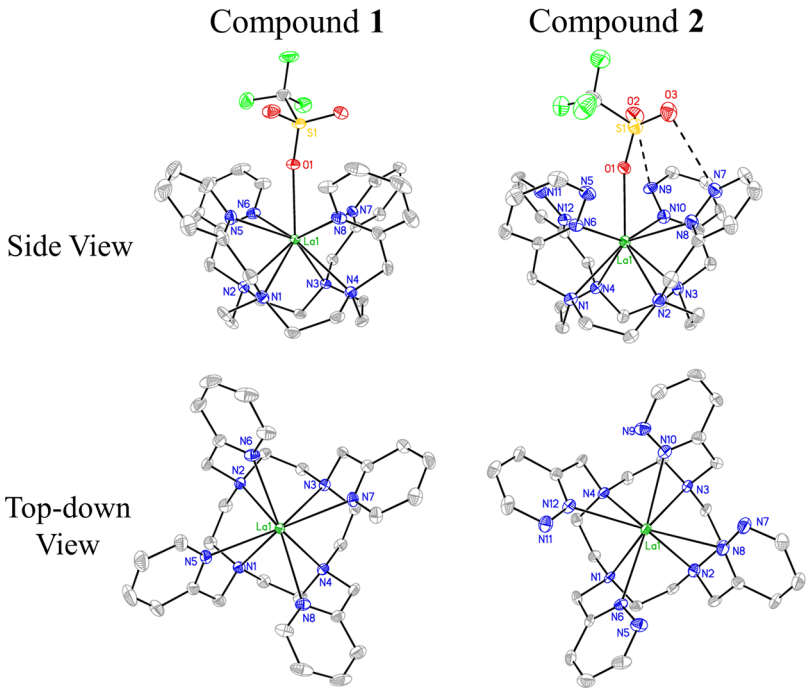

Figure 2. X-ray crystal structures of the complex cations of **1** (left) and **2** (right) from a side (top) and top-down view (bottom). The hydrogen atoms have been omitted for clarity. In the top-down perspective, the coordinated triflate ligand has also been removed. Ellipsoids are drawn at 50% probability levels.

which are not commercially available, were first prepared by the treatment of the methyl N-heterocycles with 1/3 equiv of trichloroisocyanuric acid in refluxing chloroform as previously described.[19] The chloromethyl N-heterocycles were used immediately after purification by column chromatography for the reaction with cyclen under conditions identical to those used for L^{py} to afford L^{pyd}, L^{pyr}, and L^{pz} in moderate yields (Scheme 1). Characterization data for the ligands are given in the Experimental Section and in Figures S1−S12 in the Supporting Information (SI).

The ligands were also characterized structurally in the solid state by single-crystal X-ray diffraction. The crystal structures are shown in Figure 1. Despite similar geometric requirements, all ligands crystallize with distinct unit cell parameters. As previously reported for L^{py},[18] both L^{pyd} and L^{pz} are centrosymmetric, as dictated by crystallographic inversion centers that reside in the middle of the 12-membered cyclen macrocycle. In contrast, L^{pyr} crystallizes in a puckered conformation, where the four pyrimidine heterocycles sit on the same face of the 12-membered macrocycle.

Lanthanum(III) Complex Synthesis and Characterization. To investigate the coordination chemistries of the four ligands, La^{3+} complexes were prepared. The reaction of $La(OTf)_3$ in MeOH with the ligands at 40 °C afforded complexes **1**, **2**, **3**, and **4**, which are characterized by the general formula, $[La(L)(OTf)](OTf)_2$, where OTf = trifluoromethanesulfonate and L = L^{py}, L^{pyd}, L^{pyr}, and L^{pz}, respectively. Complex **4** crystallizes out of solution directly, whereas the other three complexes are soluble in methanol. The complexes were characterized by Fourier transform infrared (FTIR) spectroscopy and elemental analysis (EA). The IR spectra (Figures S13−S16, SI) possess similar vibrational features among the four complexes, consistent with their analogous compositions. EA is consistent with the molecular formulas as well.

X-ray crystal structures of **1** and **2** are shown in Figure 2. The coordination sphere of the La^{3+} ion is comprised of the eight nitrogen donor atoms of the ligands arranged in a twisted square-antiprismatic (TSAP) geometry and a triflate counterion, which occupies the axial coordination site. Two additional triflate ions are present in the outer sphere of both structures and balance the charge of the complexes. Compound **1** is isomorphous to the corresponding Nd^{3+} and Eu^{3+} complexes of L^{py}.[18] The sum of the interatomic distances comprising the inner coordination sphere of **1** is 24.187(6) Å, whereas the Nd^{3+} and Eu^{3+} complexes have values of 23.78(2) and 23.51(4) Å, respectively. These decreases in interatomic distances upon population of the 4f orbitals in the Nd^{3+} and Eu^{3+} structures are consistent with the effects of the well-known lanthanide contraction.[20,21]

Analogous to the lanthanide complexes of DOTA,[22,23] two stable diastereomers are possible for this class of ligands. The chirality of the helical twist of the pendant carboxylate groups of DOTA and pendant N-heterocycles of the ligands studied here is denoted by Δ and Λ, respectively (Figure 3). The chirality of each of the four 5-membered chelate rings formed by the cyclen macrocycle is indicated by lowercase δ or λ (Figure 3). On the basis of these two sources of chirality, two stable diastereomers exist, namely $\Lambda(\lambda\lambda\lambda\lambda)$ and $\Lambda(\delta\delta\delta\delta)$, with the corresponding enantiomers $\Delta(\delta\delta\delta\delta)$ and $\Delta(\lambda\lambda\lambda\lambda)$. Complexes of $\Lambda(\lambda\lambda\lambda\lambda)/\Delta(\delta\delta\delta\delta)$ stereochemistry obtain a TSAP geometry. The twist angle (ϕ), which is the angle between the plane of the four nitrogen atoms on the cyclen macrocycle and the plane of the four pendant donor atoms, ranges from 20 to 30° for the TSAP isomer. For complexes of $\Lambda(\delta\delta\delta\delta)/\Delta(\lambda\lambda\lambda\lambda)$ stereochemistry, a square-antiprismatic (SAP) geometry is given, where the twist angle ranges from 36 to 45° (Figure 3). For DOTA and related ligands, the TSAP isomer is energetically preferred for the earlier lanthanide ions. The SAP geometry is stabilized in the mid to late lanthanide ions, which have smaller ionic radii.[23] The two diastereomers give rise to complexes that can have substantially

dx.doi.org/10.1021/ic501843c | Inorg. Chem. 2015, 54, 97−109

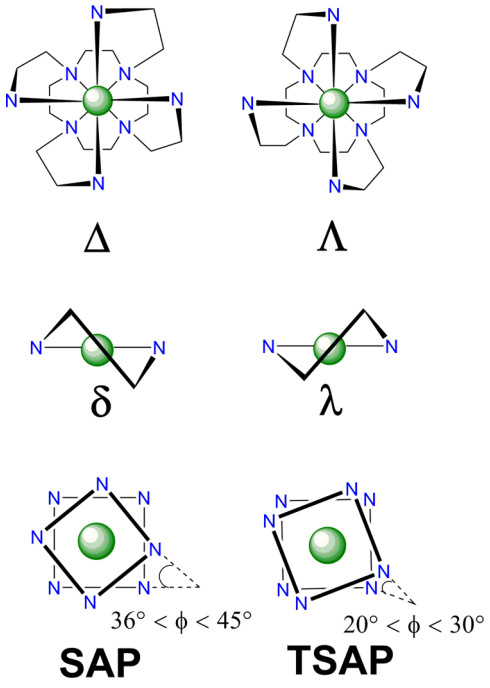

Figure 3. Schematic depiction of the sources of chirality and diastereomerism of the complexes prepared in this work.

different water-exchange rates.[24,25] Therefore, knowledge of the relative populations of these diastereomers and their rates of interconversion is crucial for the design of lanthanide complexes for luminescence and MRI sensing.

The crystal structures of **1** and **2** reveal the exclusive presence of the TSAP geometry in the solid state. Enantiomers $\Lambda(\lambda\lambda\lambda\lambda)$ and $\Delta(\delta\delta\delta\delta)$ are both present in the centrosymmetric crystal lattices of **1** and **2**. In Figure 2, the $\Lambda(\lambda\lambda\lambda\lambda)$ enantiomer of **1** and the $\Delta(\delta\delta\delta\delta)$ enantiomer of **2** are shown. TSAP geometry is expected on the basis of the large ionic radius of La^{3+}. The heavier lanthanide ions, which have small ionic radii due to the lanthanide contraction, form complexes of L^{py} with SAP geometry.[18] Specific structural data for **1**, **2**, and related La^{3+} complexes are given in Table 1. The structures and abbreviations of ligands described are given in Figure S17 of the SI. The twist angles for **1** and **2** are nearly identical (24 and 25°, respectively) and are within the expected range for TSAP geometries. La^{3+} complexes, which have twist angles that deviate significantly from this range, are $[La(DOTAM\text{-}glycol)Cl]^{2+}$ and $[La(THED)(OH_2)]^{3+}$, as indicated in Table 1. The large twist angle of $[La(DOTAM\text{-}glycol)Cl]^{2+}$ arises as a consequence of its existence in the solid state as the SAP isomer.[26] The structure of $[La(THED)(OH_2)]^{3+}$ reveals a uniquely small twist angle, which gives rise to a structure in which the pendant alcohol donor groups nearly eclipse the nitrogen atoms of the macrocycle.[27] For **1** and **2**, La–N distances are not significantly different, ranging from 2.66 to 2.75 Å. However, the average La–N_{cyclen} distances are slightly larger than the average La–$N_{pendant}$ distances for both complexes. The related La^{3+} complex, $[LaL^{2quin}(OCH_3)]^{2+}$,[28] in which the pendant N-heterocycles of **1** and **2** are replaced by 2-quinoline, is structurally similar. Notably, the La–$N_{pendant}$ distances (average 2.889(3) Å)[28] of this complex are substantially greater than those of **1** and **2**, which may possibly be a consequence of the greater steric hindrance of the quinoline arms or the strong electron-donating properties of the anionic methoxide axial ligand. The La–OTf distance of **2** is marginally smaller than that of **1**. An additional intramolecular interaction is observed in the structure of **2** as well. The two noncoordinating oxygen atoms of the triflate ligand are in close contact with the noncoordinating nitrogen atoms of the pendant pyridazine ligands (2.96 and 3.04 Å) (Figure 2). This interaction is expected to be repulsive because both nitrogen and oxygen atoms carry partial negative charges.

Crystals of **3** and **4** were also obtained. However, the quality of data afforded by these crystals was poor due to low resolution, weak intensity of reflections, and the presence of multiple twin domains. Despite these limitations, the structures could still be solved, unambiguously identifying the atomic connectivity of the complexes. In both structures, the La^{3+} ion is complexed in a TSAP fashion to the octadentate ligands and also directly coordinated to a triflate ligand in the axial position. The Supporting Information contains the measured unit cell parameters and figures depicting the atomic connectivity (Table S1 and Figures S18 and S19, SI). Although a more detailed analysis of the interatomic distances and angles cannot be carried out, these results indicate that the solid state structures of **1**–**4** are similar despite the systematic modification of the pendant N-heterocycle donor.

NMR Spectroscopy. ^{1}H and $^{13}C\{^{1}H\}$ NMR spectra of **1**–**4** in D_2O (Figures S20–S27, SI) in the temperature range of 5–95 °C reveal the presence of a single diastereomer. Based on literature precedence, X-ray crystallography (vide supra), and

Table 1. Selected Structural Parameters for 1, 2, and Related La^{3+} Complexes[a]

complex	ϕ, deg[b]	average La–N_{cyclen} distance, Å	average La–N/$O_{pendant}$ distance, Å	axial La distance, Å	La–N_4(cyclen) centroid, Å	La–O_4/N_4(pendant) centroid, Å	ref
1	23.9	2.713(4)	2.699(4)	2.5374(18)	1.71	0.83	this work
2	24.9	2.74(1)	2.69(1)	2.498(5)	1.76	0.71	this work
$[LaL^{2quin}(OCH_3)]^{2+}$[c]	24.4	2.780(3)	2.889(3)	2.149(4)	1.82	0.71	28
Na[La(HDOTA)La(DOTA)]	23.0	2.794(3)	2.493(3)	2.568(5)	1.835	0.70	29
	24.5	2.769(3)	2.492(3)	2.537(5)	1.810	0.73	
$[La(DOTAM')]^{3+}$[d]	26.7	2.718(3)	2.423(3)	N/A	1.63	1.23	30
$[La(DOTAM\text{-}glycol)Cl]^{2+}$[e]	37.7	2.788(4)	2.501(3)	2.811(3)	1.81	0.54	26
$[La(THED)(OH_2)]^{3+}$[f]	13.3	2.69(1)	2.38(2)	2.57(3)	1.68	0.95	27

[a]See Figure S17 in the SI for the structures of the ligands. [b]Twist angle; see Figure 3. [c]L^{2quin} = 1,4,7,10-tetrakis(2′-quinolylmethyl)-1,4,7,10-tetraazacyclododecane. [d]DOTAM′ = 1,4,7,10-tetrakis(2-carbamoylethyl)-l,4,7,10-tetraazacyclododecane. [e]DOTAM-glycol = 2,2′,2″,2‴-(1,4,7,10-tetraazacyclododecane-1,4,7,10-tetrayl)-tetrakis[*N*-[2-(2-hydroxyethoxy)ethyl]acetamide]. [f]THED = 1,4,7,10-tetrakis(2-hydroxyethyl)-1,4,7,10-tetraazacyclododecane.

dx.doi.org/10.1021/ic501843c | *Inorg. Chem.* 2015, 54, 97–109

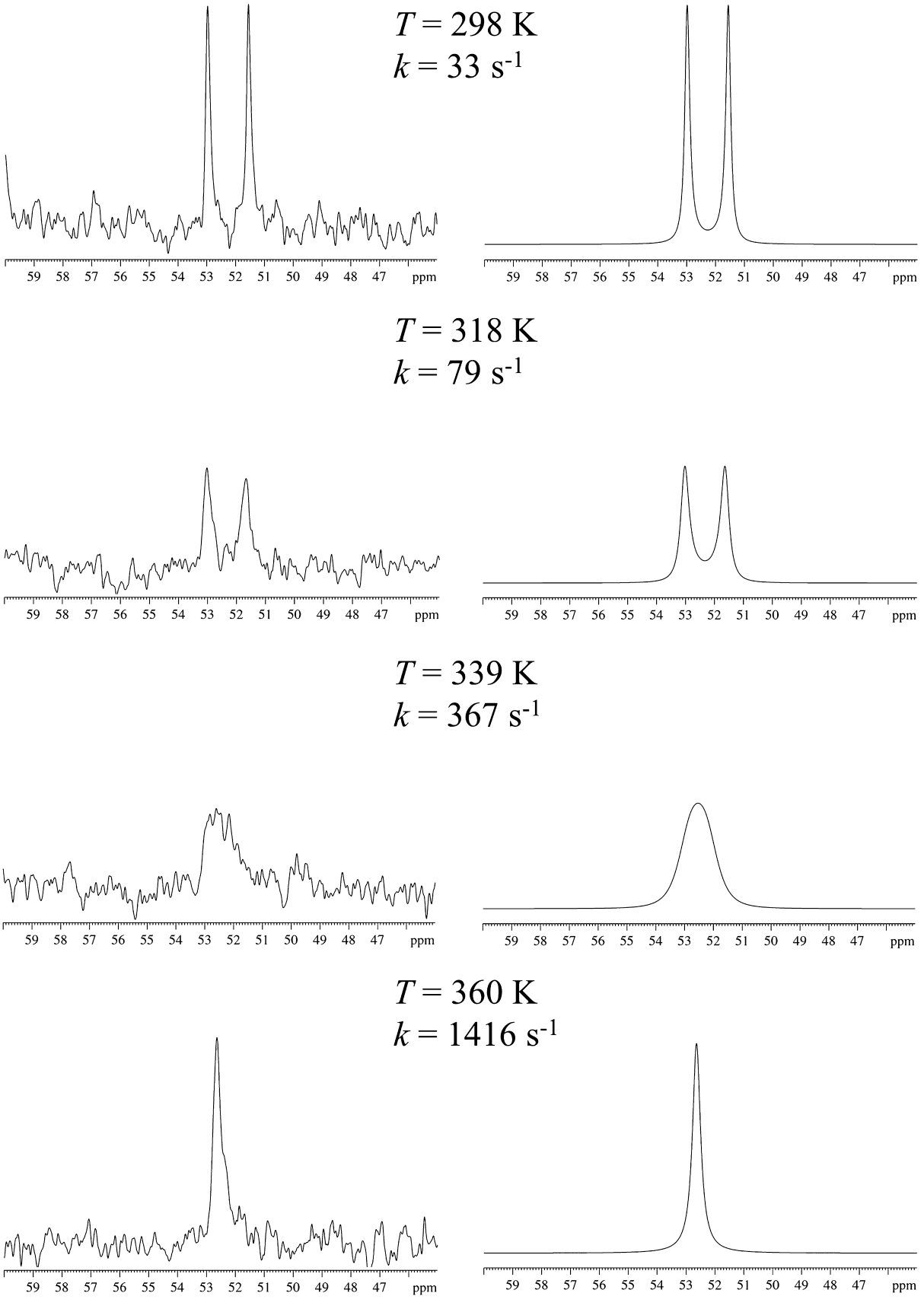

Figure 4. Variable-temperature $^{13}C\{^{1}H\}$ NMR spectra of **1** in D_2O (pD between 6 and 7, unadjusted) showing the broadening and coalescence of the resonances from the ethylenic carbon atoms on the cyclen macrocycle (left). The simulated data and corresponding rate constants are shown on the right.

dx.doi.org/10.1021/ic501843c | *Inorg. Chem.* 2015, 54, 97−109

density functional theory (DFT) calculations (vide infra), this diastereomer is most likely the TSAP isomer. The aromatic regions of both the ^{1}H and ^{13}C{^{1}H} NMR spectra for all complexes contain a single set of resonances for the pendant N-heterocycles, indicating that the complexes attain C_4 symmetry in solution. The signals arising from the aliphatic protons, however, exhibit different line widths and diastereotopic splitting among the four complexes, which suggest different degrees of conformational rigidity that depend on the nature of the ligand. Additionally, in the ^{13}C NMR spectra at 5 °C, the resonances arising from the cyclen backbone are not equivalent, further indicating that the complexes are locked into a single conformation.

The overall complex stability in aqueous solution was also assessed by NMR spectroscopy (Figures S28−S31, SI). At ambient temperature (22−25 °C) in D_2O (pD between 6 and 7, unadjusted), the ^{1}H NMR spectra were measured after 1, 7, and 24 h. Complex **1** remains stable at 24 h, with no signs of decomposition or ligand loss. Similarly, **2** displays only minor decomposition (<5%) after 24 h, as evidenced by the presence of free ligand in the ^{1}H NMR spectra. Although complexes **3** and **4** are generally stable after 1 h, as indicated by less than 5% decomposition, after longer time periods substantial decomposition is observed. At 7 h, only 86% of **3** and 67% of **4** remain intact. After 24 h, these values drop to 66% and 50% for **3** and **4**, respectively. These data indicate that the relative long-term stability of the complexes correlates with the pK_a of the pendant donor arm. Pyridine, the most basic arm, stabilizes complex **1** effectively, whereas pyrazine, the least basic arm, gives rise to poorly stable complex **4**.

Variable-temperature NMR spectroscopy was carried out to probe the conformational dynamics of the complexes in greater detail. When the temperature was increased from 5 to 95 °C, the multiplets of **1**−**4** in the aliphatic region of the ^{1}H NMR broaden and then coalesce (Figures S32−S35, SI). In the ^{13}C{^{1}H} NMR spectra, the two resonances near 53 and 60 ppm, which correspond to the ethylenic carbon atoms of the cyclen macrocycle, broaden and cleanly coalesce into a single peak as shown in Figure 4 for **1** (and Figures S36−S38 for **2**−**4**, respectively, SI). Line-shape analysis of this simple coalescence event enables extraction of first-order rate constants at different temperatures for the interconversion of these two carbon atoms. The resulting data can be evaluated with an Eyring analysis, as shown in eq 1, where k is the rate constant, T is the temperature in kelvin, R is the gas constant, k_B is the Boltzmann constant, and h is Planck's constant, to yield a straight line from which the enthalpy and entropy of activation ($\Delta H^{‡}$ and $\Delta S^{‡}$, respectively) can be calculated. A representative Eyring plot for **1** is shown in Figure 5, and those for **2**−**4** are given in Figures S39−S41, respectively, of the SI. From the $\Delta H^{‡}$ and $\Delta S^{‡}$ values, the free energy of activation ($\Delta G^{‡}$) and the first-order rate constant at 298 K were calculated according to eqs 2 and 3. These values are collected in Table 2.

$$\ln \frac{k}{T} = \frac{-\Delta H^{‡}}{RT} + \ln \frac{k_B}{h} + \frac{\Delta S^{‡}}{R} \quad (1)$$

$$\Delta G^{‡} = \Delta H^{‡} - T\Delta S^{‡} \quad (2)$$

$$k = \frac{k_B T}{h} e^{-\Delta G^{‡}/RT} \quad (3)$$

Because of the different stabilities of the complexes studied, however, line-shape analysis could be carried out only over a limited temperature range for **3** and **4**. Complete decomposition of **4** was observed upon ramping the temperature up to 95 °C, whereas approximately 67% decomposition of **3** was observed under the same conditions. Hence, the Eyring analyses for **3** and **4** were carried out only in the temperature range of 5−45 °C, temperatures at which <10% complex decomposition was observed. In contrast, complex **1** was entirely stable, and **2** exhibited only 6−10% complex degradation when the temperature was increased to 95 °C.

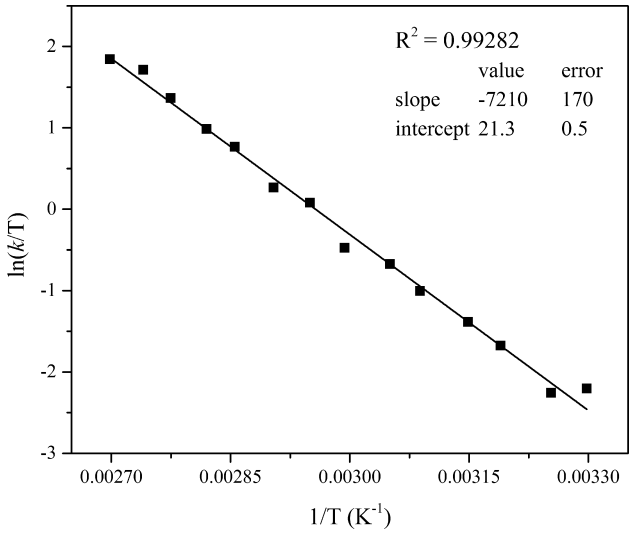

Figure 5. Eyring plot for the conformational changes observed in **1** in D_2O.

These activation parameters correspond to interconversion of the carbon atoms on the cyclen macrocycle. Because the SAP isomers of the complexes investigated here are not observed in appreciable amounts, interconversion of the carbon atoms observed at higher temperatures must correspond to a process that interconverts the two enantiomeric pairs of the TSAP isomer, $\Delta(\delta\delta\delta\delta)$ and $\Lambda(\lambda\lambda\lambda\lambda)$. This enantiomerization process can occur only through the sequential operation of two distinct processes. A ring inversion, the sequential change of the four 5-membered chelate rings from δ to λ, must take place along with concerted arm rotation of the pendant donors from Δ to Λ to interconvert the enantiomers. Line-shape analyses of the ^{13}C resonances presented here enable us to probe only the highest energy rate-determining step between both mechanisms. For complexes that form both isomers in solution, the distinct energy barriers for the arm-rotation and ring-inversion processes can be ascertained. These analyses have been carried out on diamagnetic complexes via line-shape analyses of ^{13}C resonances including those of the SAP isomer[31] and by line-shape analyses of ^{1}H NMR spectra.[32] Additionally, two-dimensional EXSY NMR spectroscopy of paramagnetic lanthanide complexes has proven valuable for the determination of activation parameters for each process.[22,24,33,34] The unobservable population of the SAP isomer for the complexes studied here, however, limits our analysis to only the highest energy barrier between both processes, corresponding to enantiomerization of the TSAP isomer, as described in earlier studies.[35−40]

The $\Delta G^{‡}$ values at 298 K vary among the four complexes from 60 to 66 kJ/mol. The changes in $\Delta H^{‡}$ and $\Delta S^{‡}$ vary more widely. Decreases in $\Delta H^{‡}$, however, are compensated for by more negative values of $\Delta S^{‡}$, leading to the relatively modest differences of $\Delta G^{‡}$ across the series. The $\Delta G^{‡}$ value for the

dx.doi.org/10.1021/ic501843c | Inorg. Chem. 2015, 54, 97−109

Table 2. Rate Constants and Activation Parameters for the Conformational Fluxionality of 1−4

	1	2	3	4
$\Delta H^{\ddagger}$, kJ mol^{-1}	60 ± 1	51 ± 1	51 ± 2	34 ± 3
$\Delta S^{\ddagger}$, J K^{-1} mol^{-1}	−20 ± 4	−30 ± 4	−40 ± 6	−93 ± 11
$\Delta G^{\ddagger}$ at 298 K, kJ mol^{-1}	66 ± 2	60 ± 2	63 ± 3	62 ± 4
k_{calcd}[a] at 298 K, s^{-1}	17	191	57	102
k[b] at 298 K, s^{-1}	33	214	52	94

[a]Obtained from combining eqs 2 and 3 and the activation parameters derived from the Eyring analysis. [b]Average value obtained from two independent line-shape analyses on two independently prepared samples.

Table 3. DFT-Calculated Structural Parameters for the TSAP Isomers of $\mathbf{1}_{H2O}$−$\mathbf{4}_{H2O}$ and 1′−4′

complex	ϕ, deg[a]	average La−N_{cyclen} distance, Å	average La−N/$O_{pendant}$ distance, Å	H_2O−La distance, Å	La−N_4(cyclen) centroid distance, Å	La−N_4(pendant) centroid distance, Å
$\mathbf{1}_{H2O}$	22.1	2.7785	2.747	2.680	1.762	0.888
$\mathbf{2}_{H2O}$	18.1	2.846	2.718	2.488	1.826	0.826
$\mathbf{3}_{H2O}$	21.5	2.785	2.7435	2.698	1.758	0.881
$\mathbf{4}_{H2O}$	21.7	2.7705	2.7695	2.682	1.742	0.917
1′	19.24	2.731	2.690		1.677	1.062
2′	17.06	2.822	2.605		1.785	0.859
3′	18.70	2.730	2.692		1.655	1.068
4′	18.50	2.721	2.712		1.656	1.102

[a]Twist angle; see Figure 3.

La^{3+} complex of DOTA is 60.7 kJ/mol,[35] which is within the range of the compounds studied here. The $\Delta G^{\ddagger}$ value of the La^{3+} complex of an analogous ligand containing two pendant carboxylate and imidazole donors is 61.5 kJ/mol, similar to that of the DOTA complex.[40] La^{3+} complexes of ligands that have neutral pendant donors, such as alcohols or amides, generally have smaller energy barriers, which range from 52 to 58.8 kJ/mol.[36−39] Although **1**−**4** contain neutral pendant donors, the energy barriers found for these complexes are more similar to those with anionic donors. This observation suggests that the steric hindrance of the large aromatic heterocycles may compensate for their lack of anionic character in enforcing more rigid conformations of the macrocyclic ligand.

A systematic decrease in both $\Delta H^{\ddagger}$ and $\Delta S^{\ddagger}$ occurs in the order of **1** > **2** > **3** > **4**. This sequence also follows that of the relative pK_a values of the pendant heterocycles, as pyridine is the most basic (pK_a 5.23), followed by pyridazine (pK_a 2.33), pyrimidine (pK_a 1.30), and pyrazine (pK_a 0.65). The large negative entropy of activation of **4**, −93 ± 11 J K^{-1} mol^{-1}, is particularly noteworthy. The La^{3+} complex of the pendant alcohol donor ligand THED (1,4,7,10-tetrakis(2-hydroxyethyl)-1,4,7,10-tetraazacyclododecane) exhibited a $\Delta S^{\ddagger}$ of −58 J K^{-1} mol^{-1},[39] and the Lu^{3+} complex of a derivative of DOTA, where the anionic carboxylate arms are replaced by neutral pendant *N*-[2-(2-hydroxyethoxy)ethyl]acetamide donors, possessed similar activation parameters as well, with $\Delta H^{\ddagger}$ = 33 ± 3 kJ/mol and $\Delta S^{\ddagger}$ = −109 ± 7 J K^{-1} mol^{-1}.[26] The observance of such a large and negative $\Delta S^{\ddagger}$ for what should be an intramolecular process was not fully explained or understood for these complexes. These $\Delta S^{\ddagger}$ values may signify an increase in symmetry in the transition state. However, the transition state also encompasses the surrounding solvent molecules whose reorganization may also significantly contribute to the overall activation parameters observed.[41] The presence of additional nitrogen atoms in the pendant heterocycles of **2**−**4** provides hydrogen-bond donors for interactions with water, which may alter the secondary solvation shell of the transition state more drastically than for that of **1**. It should also be noted that decomposition of **3** and **4** at higher temperatures limited the Eyring analysis to temperatures below the fast-exchange limit. Although the parameters determined from independent variable-temperature runs were reproducible, some additional error in the entropy of activation is most likely present, which may contribute to the large negative values observed.

DFT Calculations. Structures of the aqueous analogues of **1**−**4**, in which the inner-sphere triflate ligand is replaced by a coordinated water molecule ($\mathbf{1}_{H2O}$−$\mathbf{4}_{H2O}$), were optimized in the gas phase at the B3LYP/6-31G*/SDD(La) level of theory for both the TSAP and SAP diastereomers. The triflate ligand was replaced with a water molecule to model the most likely configuration of the complex in aqueous solution. In agreement with the crystal structure analysis, the TSAP isomers are thermodynamically preferred by 15−25 kJ/mol. This large stabilization of the TSAP isomer is consistent with our inability to observe the SAP isomer by NMR spectroscopy. Additionally, derivatives of **1**−**4** with no axial ligands, 1′−4′, were also optimized at the same level of theory. For these analogues, the TSAP isomers were stabilized to a larger degree, as indicated by free energy differences ranging from 26.6 to 33.6 kJ/mol. Selected structural parameters of the DFT-optimized TSAP diastereomers of $\mathbf{1}_{H2O}$−$\mathbf{4}_{H2O}$ and 1′−4′ are given in Table 3.

In comparison to data obtained from X-ray crystallography for **1** and **2**, the average La−N distances computed by DFT are overestimated by about 0.06 Å for $\mathbf{1}_{H2O}$ and up to 0.1 Å for $\mathbf{2}_{H2O}$. The root-mean-square deviations (RMSD) of the calculated structures overlaid with the experimentally determined structures with the axial ligand omitted are 0.1014 Å for **1** and $\mathbf{1}_{H2O}$ and 0.2854 Å for **2** and $\mathbf{2}_{H2O}$. The larger deviations observed for the DFT structure of $\mathbf{2}_{H2O}$ are most likely the result of intramolecular hydrogen bonds between the hydrogen atoms of the coordinated water molecule and the nitrogen atoms in the ortho position of the pendant pyridazine donors (Figure S42, SI). The importance of these intramolecular hydrogen bonds is most likely diminished in aqueous solution in which the water-exchange rate for lanthanide complexes occurs with lifetimes ranging from nano- to microseconds and where the presence of

dx.doi.org/10.1021/ic501843c | Inorg. Chem. 2015, 54, 97−109

outer-sphere water molecules can effectively hydrogen bond to both the coordinated water molecule and the pyridazine nitrogen atoms. The RMSD values for the overlaid structures of the structures calculated without axial ligands are 0.2199 Å for **1** and **1′** and 0.3573 Å for **2** and **2′**. These substantially larger deviations indicate that the presence of axial ligands has a dramatic effect on the coordination geometries of the La^{3+} complexes.

The activation barriers for enantiomerization of the TSAP isomers via sequential arm rotation and ring inversion of $\mathbf{1}_{H2O}$−$\mathbf{4}_{H2O}$ were also investigated. The computational approach used was similar to that developed by other researchers to investigate the solution dynamics of lanthanide complexes of DOTA and related cyclen-based macrocycles.[18,26,32,42−45] The ring-inversion mechanism, in which the chirality of each 5-membered chelate ring sequentially switches from the δ to λ configuration, was successfully modeled with DFT calculations. The relative free energies of the intermediates and transition states along this pathway in the gas phase are shown in Figure 6 for $\mathbf{1}_{H2O}$ and in

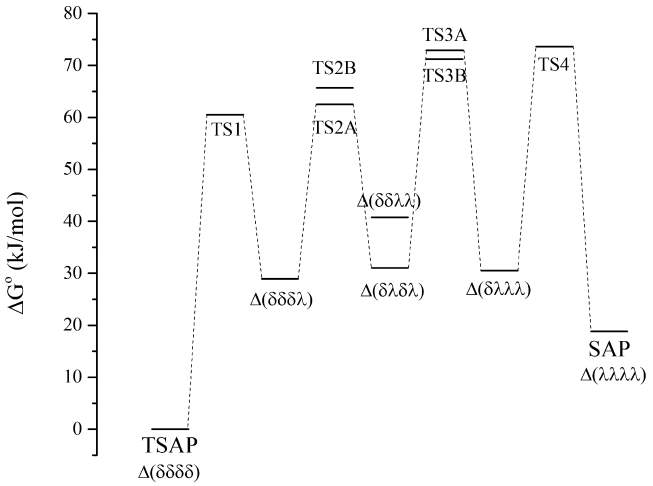

Figure 6. Relative free energies for intermediates and transition states of the ring-inversion process for $\mathbf{1}_{H2O}$ in the gas phase.

Figures S43−S45 in the SI for $\mathbf{2}_{H2O}$−$\mathbf{4}_{H2O}$, respectively. For the ring-inversion mechanism, the complexes can pass through an intermediate of either $\Delta(\delta\lambda\delta\lambda)$ or $\Delta(\delta\delta\lambda\lambda)$ stereochemistry. The highest energy barriers, however, were found to correspond to TS4 (Figure 6), suggesting that preceding intermediates of both stereochemistries are accessible during the interconversion process. Attempts to find a transition state corresponding to an arm-rotation mechanism in which the overall complex helicity switches from Δ to Λ were not successful. Therefore, the activation barriers for the complexes lacking axial ligands (**1′**−**4′**) were also computed. Transition states corresponding to the concerted arm-rotation mechanism were located in addition to those for the sequential ring-inversion mechanism. The relative gas-phase free energies of these species are shown in Figure 7 for **1′** and Figures S46−S48 in the SI for **2′**−**4′**, respectively. In Table 4, the calculated activation parameters for the highest energy barriers are reported. The highest energy barrier for all complexes in the ring inversion was found to be TS4.

Given the fast water-exchange rate of lanthanide complexes in aqueous solution, enantiomerization of the TSAP isomer could conceivably occur through complexes lacking axial ligands if these complexes provided an overall lower energy pathway. The calculated $\Delta G^{‡}$ values for **1′**−**4′** for the ring-inversion process are consistently greater than those of $\mathbf{1}_{H2O}$−$\mathbf{4}_{H2O}$ by approx-

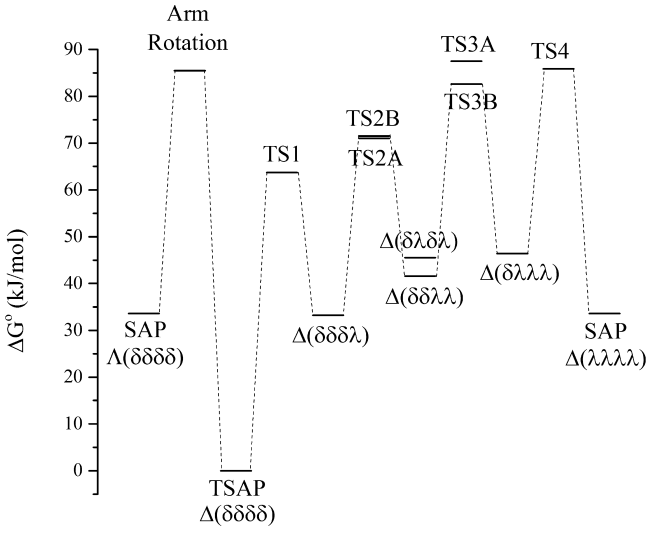

Figure 7. Relative free energies for intermediates and transition states of the ring-inversion and arm-rotation processes for **1′** in the gas phase.

imately 10 kJ/mol. The concerted arm-rotation mechanism for **2′**−**4′**, however, is energetically competitive with the ring inversion of $\mathbf{2}_{H2O}$−$\mathbf{4}_{H2O}$. In contrast, the free energy barrier of this process for **1′** is over 10 kJ/mol greater than that for the ring inversion of $\mathbf{1}_{H2O}$. Notably, the arm-rotation mechanism for **2′** has a barrier substantially smaller than that of any of the complexes studied; the computed $\Delta G^{‡}$ value at 298 K is only 44.9 kJ/mol. This small barrier may arise, in part, because of the absence of hydrogen atoms in the ortho position of the pendant heterocycle, which diminishes the unfavorable steric interactions in the transition state of the concerted arm rotation. Unfortunately, because the transition state for the arm-rotation mechanism of the hydrated complexes could not be located, these energies, which may be rate-limiting, cannot be included in this discussion.

The role of the dielectric continuum of water on the energies of all intermediates and transition states was investigated next. Attempts to optimize structures in the presence of the implicit solvation models were generally unsuccessful except for several cases. Hence, single-point calculations employing the SMD solvation model[46] were carried out on gas-phase-optimized geometries. Thermochemical corrections from the gas-phase calculations were applied to solution-phase SCF energies to estimate thermodynamic values in solution. The relative free energies in solution for $\mathbf{1}_{H2O}$ and **1′** are shown in Figures 8 and 9, respectively; the energies for $\mathbf{2}_{H2O}$−$\mathbf{4}_{H2O}$ and **2′**−**4′** are displayed in Figures S49−S54, respectively, in the SI. The pathways between the TSAP and SAP diastereomers in solution are qualitatively similar to those in the gas phase; however, intermediates and transition states are systematically destabilized in the presence of the dielectric continuum of water. The highest energy barrier in solution for the ring-inversion process is the same as that in the gas phase, TS4. Thermodynamic activation barriers for TS4 and the arm-rotation TS for **1′**−**4′** are given in Table 5. Polarization of the solvent systematically increases the activation barriers for the ring-inversion process of $\mathbf{1}_{H2O}$−$\mathbf{4}_{H2O}$ and **1′**−**4′** by 14−24 and 12−20 kJ/mol, respectively. In contrast, the $\Delta G^{‡}$ values for the arm-rotation mechanism of **1′**, **3′**, and **4′** decrease substantially due to stabilization of the transition state in a dielectric continuum. Stabilization of this transition state in solution is correlated with the dipole moment

dx.doi.org/10.1021/ic501843c | Inorg. Chem. 2015, 54, 97−109

Table 4. Activation Parameters in the Gas Phase for the Highest Energy Transition State (TS4) of the Ring-Inversion Mechanism of $\mathbf{1}_{H2O}$−$\mathbf{4}_{H2O}$ and 1′−4′ and for the Transition State of the Arm-Rotation Mechanism of 1′−4′

	ring inversion								arm rotation			
	$\mathbf{1}_{H2O}$	$\mathbf{2}_{H2O}$	$\mathbf{3}_{H2O}$	$\mathbf{4}_{H2O}$	1′	2′	3′	4′	1′	2′	3′	4′
$\Delta H^{\ddagger}$, kJ mol^{-1}	68.9	78.2	70.8	69.5	84.8	82.6	85.5	85.2	81.9	51.2	70.2	74.5
$\Delta S^{\ddagger}$, J K^{-1} mol^{-1}	−15.7	5.1	−9.6	−10	−3.8	−2.6	−3.0	−2.9	−12.3	21.2	−7.2	−9.5
$\Delta G^{\ddagger}$, kJ mol^{-1}	73.6	76.7	73.7	72.5	85.9	83.4	86.4	86.1	85.5	44.9	72.4	77.3

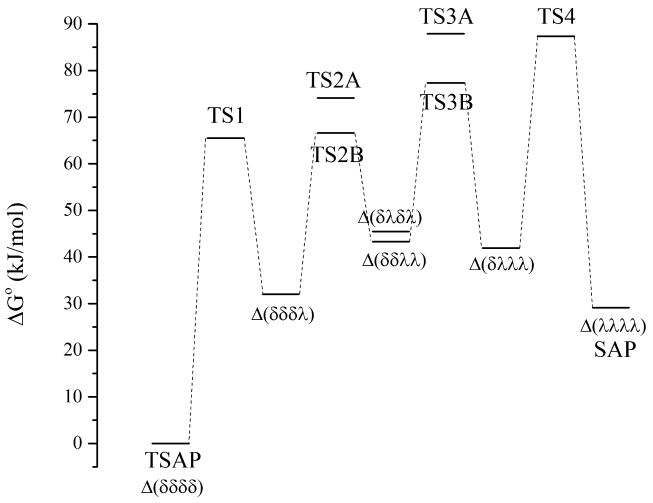

Figure 8. DFT-calculated relative free energies of transition states and intermediates for the ring-inversion process of $\mathbf{1}_{H2O}$ with the SMD solvation model applied.

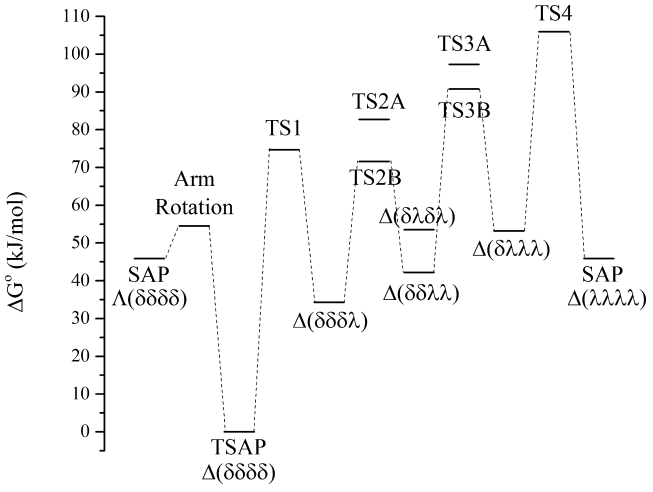

Figure 9. DFT-calculated relative free energies of transition states and intermediates for the ring-inversion and arm-rotation processes of 1′ with the SMD solvation model applied.

of the molecule; the solution-phase dipole moments of 1′, 3′, and 4′ of this transition state are more than a debye larger than those for the other intermediates and transition states along the ring-inversion pathway. In contrast, the dipole moment of the transition state for 2′ is smaller than that of the other species on the ring-inversion pathway, and therefore addition of the dielectric continuum minimally alters the energy barrier to arm rotation. The low $\Delta G^{\ddagger}$ values, all less than 60 kJ/mol, suggest that synchronous arm rotation is not the rate-limiting process for the enantiomerization process of the TSAP diastereomer. The lower energy of the ring-inversion pathway in the hydrated compared to the water-free complexes suggests that enantiomerization may occur with an axial water ligand.

The solution-phase values presented in Table 5 are generally in poorer agreement with experimental values and previously calculated values for similar systems[47] than the gas-phase calculations given in Table 4. The larger discrepancy observed by introducing solvent effects is counterintuitive. Structures of the TSAP, $\Delta(\delta\delta\delta\lambda)$, and $\Delta(\delta\lambda\delta\lambda)$ isomers of $\mathbf{1}_{H2O}$ were successfully optimized in the polarizable continuum model (PCM), along with transition states TS2A and TS3A. Other ground and transition state structures would not converge in the presence of the PCM. The calculated free energies of the PCM-optimized structures relative to the TSAP isomer are 27.8, 35.2, 63.2, and 66.9 kJ/mol for $\Delta(\delta\delta\delta\lambda)$, $\Delta(\delta\lambda\delta\lambda)$, TS2A, and TS3A, respectively. These values are in good agreement with the gas-phase calculations in which the respective values are 31.5, 31.0, 62.5, and 71.3 kJ/mol. The solution-phase energies of the gas-phase-optimized structures are, as noted above, greater than both of these sets of values at 41.9, 45.5, 74.1, and 77.3 kJ/mol for the $\Delta(\delta\delta\delta\lambda)$, $\Delta(\delta\lambda\delta\lambda)$, TS2A, and TS3A structures, respectively. Therefore, it appears that because the geometries were not allowed to relax in the potential energy surface of the PCM, a systematic error is introduced, which manifests in the larger than expected barriers and energy values relative to the TSAP isomer. The decrease in the energy of the transition state of the arm-rotation mechanism, however, is a significant insight that is granted only by the introduction of the solvation model. Thus, the use of these single-point solvation energy calculations is still capable of giving valuable qualitative insights.

The experimentally determined activation parameters for **1** ($\Delta H^{\ddagger}$ = 60 kJ/mol, $\Delta S^{\ddagger}$ = −20 J K^{-1} mol^{-1}) are in close agreement with the calculated solution-phase ring-inversion

Table 5. Activation Parameters in Water Using the SMD Solvation Model for the Highest Energy Transition State (TS4) of the Ring-Inversion Mechanism of $\mathbf{1}_{H2O}$−$\mathbf{4}_{H2O}$ and 1′−4′ and for the Transition State of the Arm-Rotation Mechanism of 1′−4′[a]

	ring inversion								arm rotation			
	$\mathbf{1}_{H2O}$	$\mathbf{2}_{H2O}$	$\mathbf{3}_{H2O}$	$\mathbf{4}_{H2O}$	1′	2′	3′	4′	1′	2′	3′	4′
$\Delta H^{\ddagger}$, kJ mol^{-1}	82.7	99.1	82.8	93.9	104.7	93.9	104.2	104.0	50.8	63.0	44.7	44.9
$\Delta S^{\ddagger}$, J K^{-1} mol^{-1}	−15.7	5.1	−9.6	−10	−3.8	−2.6	−3.0	−2.9	−12.3	21.2	−7.2	−9.5
$\Delta G^{\ddagger}$, kJ mol^{-1}	87.4	97.6	85.6	96.9	105.8	94.6	105.1	104.8	54.5	56.7	46.8	42.1

[a]Entropy and enthalpy corrections were used from the corresponding gas-phase calculations.

dx.doi.org/10.1021/ic501843c | Inorg. Chem. 2015, 54, 97−109

barrier of $\mathbf{1}_{H2O}$ and arm rotation of $\mathbf{1}'$. The $\Delta S^{\ddagger}$ values are of the expected sign and magnitude. In contrast, the larger, more negative $\Delta S^{\ddagger}$ values determined experimentally for **2**−**4** are not matched well by the DFT calculations. This poor agreement may arise from a lack of consideration for explicit solvent molecules, which may be the determining factors in the entropy of activation values.

SUMMARY AND CONCLUSIONS

A series of nitrogen-rich macrocyclic ligands were prepared. The pendant donors were systematically varied to provide a series of structurally homologous yet electronically distinct ligands. The coordination chemistry of these ligands with La^{3+} revealed that subtle modifications of the ligand donors gave rise to differing degrees of conformational rigidity and thermal stability of the resulting complexes in solution. More basic pendant donors gave rise to more thermally stable complexes. This parameter, however, did not correlate with the conformational rigidity of the complexes in solution. DFT calculations, employed to investigate the conformational dynamics of these complexes in solution, were carried out. These calculations in the gas phase reveal good agreement with experimental data, implicating the ring-inversion mechanism as the rate-determining step for enantiomerization. The broader utility of this new class of nitrogen-rich octadentate ligands for the chelation of medical radioisotopes is currently under investigation.

EXPERIMENTAL SECTION

Materials and Methods. Solvents used were of analytical grade. Cs_2CO_3 was purchased from Acrös Organics, and cyclen and $La(OTf)_3$ were procured from Strem Chemicals. The ligand L^{py} was synthesized as previously reported.[18] The chloromethyl N-heterocycles were synthesized by the reaction of trichloroisocyanuric acid and the methyl N-heterocycle and were purified by SiO_2 gel column chromatography, eluting with either 100% ethyl acetate or 100% diethyl ether (stabilized with 1−2% ethanol) as previously described.[19] The residual solvent content in these products, which are viscous oils, was quantified by NMR spectroscopy and incorporated in the molecular weight used for calculating proper stoichiometric quantities. Reactions were carried out under normal atmospheric conditions with no efforts to exclude atmospheric moisture or oxygen.

Physical Measurements. Fourier transform infrared (FTIR) spectra were acquired with a Thermo Scientific Nicolet iS10 spectrometer in the attenuated total reflectance (ATR) mode with a diamond ATR crystal accessory. Relative peak intensities are reported as very strong (vs), strong (s), medium (m), weak (w), or very weak (vw). APCI-MS data were acquired with a Varian 500-MS Ion Trap Mass Spectrometer with the capillary and needle voltages set to 95 and 4055 V, respectively. Elemental analyses (CHN) were performed by ALS Environmental (Tucson, AZ). NMR spectra were acquired with a Bruker Avance III HD 400 MHz Spectrometer interfaced with TopSpin v3.2 software. In deuterated organic solvents, chemical shifts were referenced internally to residual protic solvent peaks. For NMR spectra acquired in D_2O, shifts were referenced internally to either residual acetonitrile (δ^1H = 2.22 ppm, δ^{13}C (CH_3) = 1.97 ppm) or a small amount of added 1,4-dioxane (δ^1H = 3.75 ppm, δ^{13}C = 67.19 ppm).[48] For variable-temperature experiments, the temperatures were corrected using an ethylene glycol chemical shift thermometer.[49] Correction factors were generally less than 1 K. Samples of **1**−**4** were prepared in D_2O at concentrations of 25−50 mM. The pD values of the solutions were not adjusted but were found to be consistently between 6.0 and 7.0 with pH paper. Line-shape analysis of the two coalescing ^{13}C resonances was carried out using the DNMR module of Bruker's TopSpin v3.2 software. Variable-temperature runs were carried out two times with independently prepared samples. The data from the two runs were combined on a single Eyring plot. Errors quoted are derived from the standard errors of the least-squares fit to the linear equation. Eyring analyses of **3** and **4** were complicated by the observation of significant complex decomposition at temperatures greater than 45 °C. Therefore, line-shape analysis was carried out only in the 5−45 °C range. Because this narrow temperature range precludes the analysis of rate constants near and above the coalescence temperature, a greater error was associated with the Eyring analyses of these two complexes as reflected by poorer linear fits.

1,4,7,10-Tetrakis(3-pyridazylmethyl)-1,4,7,10-tetraazacyclododecane (L^{pyd}). To a mixture of 233 mg (1.35 mmol) of cyclen and 8.8 g (27 mmol) of Cs_2CO_3 in 6 mL of CH_3CN was added a solution of 3-(chloromethyl)pyridazine·3.6EtOH (1.67 g, 6.57 mmol) in 9 mL of CH_3CN in a dropwise manner. The resulting suspension was then heated to reflux for 16 h. The dark orange-brown mixture was filtered through a pad of Celite while still hot. The solid residue, remaining on the Celite pad, was washed with 5 × 5 mL of boiling CH_3CN until the eluate was colorless. The combined filtrate and washings were evaporated to dryness under reduced pressure at 40 °C, leaving a brown residue. The residue was taken up in 3 mL of CH_3CN. The red-brown supernatant was carefully separated from the beige solid with a Pasteur pipet, and the solid was washed an additional three times with 3 mL of CH_3CN. The solid was then dissolved in 10 mL of boiling CH_3CN, and the resulting orange solution was filtered through a column of Celite while still hot to remove some solid impurities. The filtrate was stored at −20 °C for 5 h, giving rise to pale-orange crystals of the desired compound. The supernatant was decanted from the crystals, which were washed sequentially with 3 × 5 mL of cold (−20 °C) CH_3CN and 3 × 5 mL of Et_2O and then dried in air. Yield: 315 mg, 43%. ^{1}H NMR (400 MHz, $CDCl_3$, 25 °C): δ 9.04 (4H, d), 7.65 (4H, d), 7.35 (4H, dd), 3.78 (8H, s), 2.75 (16H, s). ^{13}C{^{1}H} NMR (100 MHz, $CDCl_3$, 25 °C): δ 161.9, 150.5, 127.0, 126.6, 59.6, 53.3. IR (ATR, cm^{-1}): 2938 w, 2824 m, 2785 m, 5179 m, 1555 w, 1453 s, 1431 s, 1399 s, 1371 s, 1355 s, 1307 s, 1288 s, 1265 s, 1250 s, 1185 m, 1152 m, 1133 s, 1094 s, 1079 s, 1068 s, 1046 s, 1008 s, 996 s, 961 m, 923 s, 844 w, 823 s, 780 s, 749 s. APCI-MS (positive ion mode, MeOH) m/z: 541.5; calcd for $[M + H]^+$, 541.3. Anal. Calcd for $C_{28}H_{36}N_{12}$ (L^{pyd}): C, 62.20; H, 6.71; N, 31.09. Found: C, 62.34; H, 6.75; N, 30.96.

1,4,7,10-Tetrakis(4-pyrimidylmethyl)-1,4,7,10-tetraazacyclododecane (L^{pyr}). To a mixture of 517 mg (3.00 mmol) of cyclen and 20.5 g (62.9 mmol) of Cs_2CO_3 in 15 mL of CH_3CN was added a solution of 4-(chloromethyl)pyrimidine·0.75EtOAc (2.45 g, 12.6 mmol) in 10 mL of CH_3CN in a dropwise manner. The resulting suspension was then heated to reflux for 16 h. The dark red-orange mixture was filtered through a pad of Celite while still hot. The pale-brown solid residue, remaining on the Celite pad, was washed with 5 × 5 mL of boiling CH_3CN until the eluate was colorless. The combined filtrate and washings were evaporated to dryness under reduced pressure at 40 °C, leaving a red oily residue. The residue was taken up in 5 mL of CH_3CN and cooled in an ice bath for 15 min. A pale-orange solid was separated from the dark red solution by decanting. The remaining solid was washed with 2 × 5 mL of CH_3CN and then dissolved in 16 mL of boiling CH_3CN. The orange-red solution was filtered through a column of Celite while still hot and then stored at −20 °C for 16 h. A pale-orange crystalline solid deposited, which was separated from the orange supernatant by decanting. The solid was washed sequentially with 3 × 2 mL of cold (−20 °C) CH_3CN and 3 × 2 mL of Et_2O and then dried in air. Yield: 594 mg, 37%. ^{1}H NMR (400 MHz, $CDCl_3$, 25 °C): δ 9.08 (4H, s), 8.51 (4H, d), 7.69 (4H, d), 3.62 (8H, s), 2.78 (16H, s). ^{13}C{^{1}H} NMR (100 MHz, $CDCl_3$, 25 °C): δ 168.8, 158.7, 157.1, 120.1, 60.9, 53.8. IR (ATR, cm^{-1}): 2794 m, 1578 vs, 1548 s, 1471 m, 1436 m, 1384 s, 1360 s, 1307 m, 1293 s, 1248 m, 1158 w, 1108 s, 1071 w, 994 m, 973 m, 902 s, 869 s, 834 s, 798 s, 777 s, 739 s, 677 m. APCI-MS (positive ion mode, MeOH) m/z: 541.2; calcd for $[M + H]^+$, 541.3. Anal. Calcd for $C_{28}H_{36}N_{12}$ (L^{pyr}): C, 62.20; H, 6.71; N, 31.09. Found: C, 61.88; H, 6.78; N, 30.75.

1,4,7,10-Tetrakis(2-pyrazinylmethyl)-1,4,7,10-tetraazacyclododecane (L^{pz}). To a mixture of 333 mg (1.93 mmol) of cyclen and 13.0 g (39.9 mmol) of Cs_2CO_3 in 15 mL of CH_3CN was added a solution of 2-(chloromethyl)pyrazine·0.13EtOH (1.14 g, 8.48 mmol) in 10 mL of CH_3CN in a dropwise manner. The resulting suspension was

dx.doi.org/10.1021/ic501843c | Inorg. Chem. 2015, 54, 97−109

Table 6. X-ray Crystallographic Data Collection and Refinement Parameters

	L^{pyd}	L^{pyr}	L^{pz}	**1**·0.5Et_2O	**2**·H_2O
formula	$C_{28}H_{36}N_{12}$	$C_{28}H_{36}N_{12}$	$C_{28}H_{36}N_{12}$	$C_{41}H_{51}F_9LaN_{10}O_{9.50}S_3$	$C_{33}H_{39}F_9LaN_{13}O_{10}S_3$
fw	540.69	540.69	540.69	1242.01	1183.86
space group	$P\bar{1}$	$Pna2_1$	$P2_1/n$	$Pbcn$	$P2_1/n$
a, Å	8.8576(5)	16.343(5)	11.6230(15)	34.084(5)	12.945(4)
b, Å	9.6141(6)	12.689(4)	10.0308(13)	13.3725(19)	27.498(8)
c, Å	9.6564(6)	13.491(4)	11.6987(15)	21.967(3)	13.200(4)
α, deg	106.408(4)				
β, deg	91.713(4)		99.7720(10)		91.262(4)
γ, deg	115.409(4)				
V, Å^3	701.61(7)	2797.8(14)	1344.1(3)	10012(2)	4698(2)
Z	1	4	2	8	4
ρ_{calcd}, g cm^3	1.280	1.284	1.336	1.648	1.674
T, K	140(2)	140(2)	140(2)	140(2)	140(2)
μ (Mo Kα), mm^{-1}	0.083	0.083	0.086	1.076	1.145
θ range, deg	2.23−28.87	2.03−25.12	2.28−27.48	1.85−27.24	1.48−25.13
total data	16845	25569	14616	106007	53829
unique data	3637	4970	3055	11193	8352
parameters	181	361	181	675	636
restraints	0	1	0	38	25
completeness, %	99.0	99.9	99.5	99.8	99.2
R_1,[a] %	5.09	3.24	3.69	3.17	6.41
wR_2,[b] %	9.40	6.93	9.28	7.34	15.83
GoF[c]	1.011	1.033	1.039	1.051	1.060
max, min peaks, e Å^{-3}	0.276, −0.237	0.160, −0.168	0.301, −0.244	1.436, −0.843	1.709, −1.096

[a] $R_1 = \sum||F_o| - |F_c||/\sum|F_o|$ for $I > 2\sigma$. [b] $wR_2 = \{\sum[w(F_o^2 - F_c^2)^2]/\sum[w(F_o^2)^2]\}^{1/2}$ for $I > 2\sigma$. [c] GoF = $\{\sum[w(F_o^2 - F_c^2)^2]/(n-p)\}^{1/2}$, where n is the number of data points and p is the number of refined parameters.

then heated to reflux for 16 h. The yellow-brown mixture was filtered through a pad of Celite while still hot. The pale brown solid residue, remaining on the Celite pad, was washed with 3 × 5 mL of boiling CH_3CN. The combined orange filtrate and washings were stored at −20 °C for 4 h. The mix was then filtered to collect the product as an off-white crystalline solid. The solid was washed sequentially with 3 × 5 mL of cold (−20 °C) CH_3CN and 3 × 5 mL of Et_2O and then dried in air. Yield: 639 mg, 61%. ^{1}H NMR (400 MHz, $CDCl_3$, 25 °C): δ 8.78 (4H, s), 8.43 (8H, d+d), 3.65 (8H, s), 2.76 (16H, s). $^{13}C\{^1H\}$ NMR (100 MHz, $CDCl_3$, 25 °C): δ 155.3, 145.7, 143.8, 143.2, 59.6, 53.6. IR (ATR, cm^{-1}): 2947 w, 2802 m, 1479 w, 1455 m, 1430 m, 1397 s, 1369 s, 1353 s, 1308 vs, 1295 m, 1233 w, 1154 m, 1134 s, 1081 vs, 1064 m, 1049 m, 1013 s, 924 s, 859 s, 830 s, 803 m, 749 w, 660 w. APCI-MS (positive ion mode, MeOH) m/z: 541.5; calcd for $[M + H]^+$, 541.3. Anal. Calcd for $C_{28}H_{36}N_{12}$ (L^{pz}): C, 62.20; H, 6.71; N, 31.09. Found: C, 62.24; H, 6.78; N, 30.88.

[LaL^{py}(OTf)](OTf)$_2$ (1). A solution of L^{py} (46 mg, 0.086 mmol) in 5 mL of MeOH was added in a dropwise manner to a solution of La(OTf)$_3$ (50 mg, 0.085 mmol) in 5 mL of MeOH. The combined reagents were then heated at 40 °C for 3 h. The colorless solution was concentrated to dryness under vacuum at 40 °C to give a white oily residue. The residue was dissolved in 1 mL of CH_3CN. The slow vapor diffusion of Et_2O at room temperature into this solution afforded needle-like colorless crystals of the desired compound. The crystals were washed with 3 × 1 mL of Et_2O and then dried in vacuo. Yield: 71 mg, 74%. ^{1}H NMR (400 MHz, D_2O, 5 °C): δ 8.12 (4H, t), 7.84 (4H, d), 7.68 (4H, d), 7.43 (4H, t), 4.54 (4H, d), 4.01 (4H, t), 3.85 (4H, d), 3.33 (4H, t), 2.71 (8H, t). $^{13}C\{^1H\}$ NMR (100 MHz, D_2O, 5 °C): δ 157.9, 149.4, 142.8, 126.8, 125.8, 120.6 (q, $^1J_{CF}$ = 315 Hz), 60.6, 53.4, 51.9. IR (ATR, cm^{-1}): 2867 w, 1607 m, 1571 m, 1483 m, 1444 m, 1380 w, 1313 m, 1254 s, 1209 s, 1153 s, 1076 m, 1024 vs, 974 m, 907 w, 839 w, 812 m, 780 m, 758 s, 731 w. Anal. Calcd for $C_{35}H_{40}N_8F_9LaO_9S_3$ (**1**): C, 37.44; H, 3.59; N, 9.98. Found: C, 37.11; H, 3.87; N, 9.80.

[LaL^{pyd}(OTf)](OTf)$_2$·H$_2$O (2·H$_2$O). A solution of L^{pyd} (87 mg, 0.16 mmol) in 2 mL of MeOH was added in a dropwise manner to a solution of La(OTf)$_3$ (94 mg, 0.16 mmol) in 3 mL of MeOH. The combined reagents were then heated at 40 °C for 6 h. The pale yellow solution was concentrated to dryness under vacuum at 40 °C to give an oily orange residue. The residue was dissolved in 1.5 mL of CH_3CN and filtered. Slow vapor diffusion of Et_2O at room temperature into this solution afforded a pale yellow crystalline solid. This solid was dispersed in 1 mL of CH_3CN and then centrifuged. The solid, now white in color, was separated from the yellow supernatant, washed with 1.5 mL of CH_3CN and 3 × 1 mL of Et_2O, and dried in vacuo. Et_2O was allowed to vapor diffuse into the yellow supernatant, affording an additional crop of white crystalline product, which was washed with 3 × 1 mL of Et_2O, and dried in vacuo. Yield: 40 mg (first crop) + 26 mg (second crop), 36%. ^{1}H NMR (400 MHz, D_2O, 5 °C): δ 8.98 (4H, t), 7.94 (8H, d+d), 4.57 (4H, br d), 4.02 (8H, br t), 3.52 (4H, br t), 2.80 (8H, br d). $^{13}C\{^1H\}$ NMR (100 MHz, D_2O, 5 °C): δ 162.6, 152.7, 132.3, 131.1, 120.2 (q, $^1J_{CF}$ = 316 Hz), 59.0, 53.71 (br), 51.43 (br). IR (ATR, cm^{-1}): 3069 w, 2862 w, 1616 w, 1595 m, 1560 w, 1483 w, 1443 m, 1415 w, 1367 vw, 1251 vs, 1221 s, 1151 s, 1076 m, 1027 vs, 1007 s, 967 m, 904 w, 839 m, 815 m, 772 w, 756 w, 745 w. Anal. Calcd for $C_{31}H_{38}N_{12}F_9LaO_{10}S_3$ (**2**·H_2O): C, 32.52; H, 3.35; N, 14.68. Found: C, 32.47; H, 3.59; N, 14.59.

[LaL^{pyr}(OTf)](OTf)$_2$·MeOH (3·MeOH). A solution of L^{pyr} (100 mg, 0.18 mmol) in 3 mL of MeOH was added in a dropwise manner to a solution of La(OTf)$_3$ (108 mg, 0.18 mmol) in 3 mL of MeOH. The combined reagents were then heated at 40 °C for 6 h and then allowed to cool to room temperature. Vapor diffusion of Et_2O at room temperature into the resulting yellow solution afforded a white crystalline solid. The supernatant was decanted, and the solid was washed with 3 × 2 mL of Et_2O and dried in vacuo. Yield: 130 mg, 62%. ^{1}H NMR (400 MHz, D_2O, 5 °C): δ 9.03 (4H, d), 8.55 (4H, s), 7.86 (4H, d), 4.64 (4H, d), 4.04 (8H, m), 3.26 (4H, t), 2.81 (8H, m). $^{13}C\{^1H\}$ NMR (100 MHz, D_2O, 5 °C): δ 166.7, 161.7, 158.3, 123.8, 120.2 (q, $^1J_{CF}$ = 315 Hz), 59.8, 53.6, 51.3. IR (ATR, cm^{-1}): 2873 w, 1593 s, 1554 m, 1483 w, 1460 w, 1400 m, 1312 m, 1253 vs, 1207 s, 1155 s, 1075 m, 1026 vs, 1002 m, 966 m, 906 s, 839 w, 812 w, 779 w, 740 w, 688 m. Anal. Calcd for $C_{32}H_{40}N_{12}F_9LaO_{10}S_3$ (**3**·MeOH): C, 33.17; H, 3.48; N, 14.50. Found: C, 33.73; H, 3.74; N, 14.81.

[LaL^{pz}(OTf)](OTf)$_2$·MeOH (4·MeOH). L^{pz} (50 mg, 0.092 mmol) was dissolved in 2 mL of MeOH by heating the mixture to 50 °C. The resulting solution of L^{pz} was added to La(OTf)$_3$ (54 mg, 0.092 mmol)

dx.doi.org/10.1021/ic501843c | Inorg. Chem. 2015, 54, 97−109

dissolved in 0.5 mL of MeOH. After the solution had sat at room temperature for 16 h without being stirred, colorless plate-like crystals of the desired compound deposited. The supernatant was carefully removed with a Pasteur pipet, and the crystals were washed sequentially with 3 × 2 mL of hot (40 °C) MeOH and 3 × 2 mL of Et_2O. The remaining solid was dried in vacuo at room temperature. Yield: 27 mg, 25%. ^{1}H NMR (400 MHz, D_2O, 5 °C): δ 8.67 (4H, s), 8.64 (4H, d), 8.17 (4H, unresolved d), 4.44 (4H, d), 3.92 (8H, d), 3.22 (4H, br t), 2.66 (8H, br t). ^{13}C{^{1}H} NMR (100 MHz, D_2O, 5 °C): δ 152.8, 147.0, 145.7, 144.5, 120.2 (q, $^1J_{CF}$ = 315 Hz), 57.8, 53.1, 51.0. IR (ATR, cm^{-1}): 2862 w, 1481 w, 1458 w, 1420 w, 1374 w, 1255 vs, 1222 m, 1150 s, 1080 m, 1027 vs, 1007 m, 968 w, 902 w, 855 w, 840 w, 803 w, 774 w, 752 w, 676 w. Anal. Calcd for $C_{32}H_{40}N_{12}F_9LaO_{10}S_3$ (**4**·MeOH): C, 33.17; H, 3.48; N, 14.50. Found: C, 32.70; H, 3.95; N, 14.59.

X-ray Crystallography. Single crystals of L^{pyd} and L^{pyr} were obtained by the slow evaporation of methanolic solutions, whereas crystals of L^{pz} were grown by vapor diffusion of Et_2O into a dimethylformamide solution. Vapor diffusion of Et_2O into CH_3CN solutions of **1** and **2** afforded X-ray quality crystals. Weakly diffracting and highly twinned crystals of **3** and **4** were obtained by the vapor diffusion of Et_2O into a methanolic solution and directly from the methanol reaction solvent, respectively.

Single crystals were mounted on a nylon loop in *n*-paratone oil and cooled with a Bruker Kryoflex nitrogen cold stream. A Bruker D8 diffractometer with a graphite monochromatized Mo Kα X-ray source (λ = 0.71073 Å) controlled by the *APEX2* software package[50] was used for data collection. Data were integrated with *SAINT*[51] and subsequently corrected for absorption with *SADABS*.[51] The *SHELXTL* software package[52,53] was employed for structure solution and refinement against F^2. Heavy atoms were located on the difference Fourier map and refined anisotropically. Hydrogen atoms were placed at calculated positions and given isotropic thermal parameters equal to either 1.5 (terminal CH_3 groups) or 1.2 times that of the thermal parameter of the atom to which they were attached. For the ligands L^{pyd}, L^{pyr}, and L^{pz}, the locations of the nitrogen atoms on the heterocycles were assigned by careful analysis of the difference Fourier map prior to hydrogen atom placement. No electron density corresponding to hydrogen atoms was located at the atoms assigned as nitrogens, whereas the other atoms on the heterocycle clearly displayed residual density arising from hydrogens. L^{pyr} crystallized in the noncentrosymmetric space group $Pna2_1$. Because of the lack of heavy atoms in the structure of L^{pyr}, the absolute structure was not refined. In the structure of **1**, the oxygen atom of a disordered molecule of diethyl ether was located on a crystallographic 2-fold axis. The geometries of the disordered components were refined with similarity restraints (SADI, default values), and the sum of the occupancy of the components was constrained to unity. The thermal displacement parameters of this disordered molecule were also restrained to have similar size and shape (SIMU and DELU, default values). For **2**, after all species in the asymmetric unit had been identified and assigned, several peaks of residual electron density remained. The electron density was refined as four water molecules, disordered spatially within this void. The sum of the occupancy of the four oxygen atoms was constrained to unity. The thermal ellipsoids of the oxygen atoms were restrained to be spherical (ISOR, default values) and constrained to be identical (EADP). Because of the low occupancy of each oxygen atom, hydrogen atoms were neither located on the difference Fourier map nor included in the final model. X-ray crystallographic data collection and refinement parameters are collected in Table 6, and CIF files can be found in the SI. The poor quality data sets afforded from crystals of **3** and **4** were not amenable to satisfactory structure refinement. Structure solution, however, was carried out, and basic atomic connectivity could be resolved. The unit cell parameters and space groups used for resolution of these structures are given in Table S1 of the SI.

DFT Calculations. DFT calculations were carried out with the *Gaussian09* software package.[54] The hybrid functional B3LYP[55,56] was used, and the Pople-style basis set 6-31G(d)[57,58] was assigned to atoms other than La. For La, the quasi-relativistic 28-electron Stuttgart/Dresden (SDD) effective core potential[59] was employed. The associated segmented SDD basis set[60] was modified for computational efficiency by removing the *g* functions and removing the most diffuse functions (those with exponential constants <0.05). Geometries of both stable structures and transition states were optimized in the gas phase. Transition-state structures were obtained using the synchronous transit-guided quasi-Newton method.[61,62] Intermediates and transition states were characterized by frequency calculations, which gave zero-point energy-corrected thermodynamic values. Intermediates possessed no imaginary frequencies, which verified their position at a local minimum on the potential energy surface. Transition states contained a single imaginary frequency. The imaginary frequency was visualized with *GaussView5* to confirm that it traversed the proper reaction coordinates between two intermediates. Solution energies in water were calculated using the implicit SMD solvation model.[46] Single-point energy calculations of gas-phase-optimized structures were carried out in the dielectric continuum. The thermochemical correction factors obtained from gas-phase frequency analyses were applied to the SCF energy of the same structure in solution to estimate thermodynamic parameters. The thermal correction to Gibbs free energy was modified for a pressure of 1354 atm on the basis of the experimental density of liquid water prior to adjustment of the SCF energy in solution.[63] Gas-phase thermochemical calculations employed a pressure of 1 atm. All free energy values cited throughout the Article are calculated at 298 K unless otherwise stated. For two transition state structures, those of the arm-rotation mechanism of **2′** and of TS4 of **3′**, stationary points were not found with the default optimization criteria of *Gaussian09*. Whereas the maximum force and RMS converged, the maximum displacement and its RMS remained above the convergence criteria. Calculating exact force constants at each step, decreasing the optimization step size, and carrying out the optimization in Cartesian coordinates failed to give geometries that satisfied the maximum displacement convergence criteria. Variations in electronic energies during the optimizations of the arm-rotation transition state of **2′** and TS4 of **3′** were only 0.00015 hartree (0.4 kJ/mol) and 0.0004 hartree (1 kJ/mol), respectively. Frequency calculations on the final geometries obtained after exceeding the maximum number of steps were carried out. Only a single imaginary frequency corresponding to the desired reaction coordinate was obtained for both structures. The thermochemical data for these incompletely optimized structures were used for the analysis described above. Coordinates and energies for both the gas phase and in solution of all optimized structures are given in Tables S2−S101 in the SI.

■ ASSOCIATED CONTENT

Supporting Information

X-ray crystallographic data in CIF format, complete characterization data, Eyring analyses, and DFT energies and optimized coordinates. This material is available free of charge via the Internet at http://pubs.acs.org.

■ AUTHOR INFORMATION

Corresponding Authors

*E-mail: jjwilson@lanl.gov.
*E-mail: eva@lanl.gov.

Notes

The authors declare no competing financial interest.

■ ACKNOWLEDGMENTS

We thank Dr. Ben Davis for assistance with and use of a mass spectrometer. J.J.W. acknowledges funding support via the LANL/LDRD program through a Seaborg Institute Postdoctoral Research Fellowship. The research described in this paper was funded by the United States Department of Energy Office of Science via funding from the Isotope Development and Production for Research and Applications subprogram in the Office of Science, Nuclear Physics, and through the Heavy Element Chemistry Program of BES (R. L. Martin and E. R. Batista). The content of this Article has been reviewed and approved for public release as LA-UR-14-25841.

REFERENCES

(1) Liu, S.; Edwards, D. S. *Bioconjugate Chem.* **2001**, *12*, 7.
(2) Parker, D.; Dickins, R. S.; Puschmann, H.; Crossland, C.; Howard, J. A. K. *Chem. Rev.* **2002**, *102*, 1977.
(3) Gunnlaugsson, T.; Leonard, J. P. *Chem. Commun. (Cambridge, U.K.)* **2005**, 3114.
(4) Bottrill, M.; Kwok, L.; Long, N. J. *Chem. Soc. Rev.* **2006**, *35*, 557.
(5) Bünzli, J.-C. G.; Eliseeva, S. V. *Chem. Sci.* **2013**, *4*, 1939.
(6) Heffern, M. C.; Matosziuk, L. M.; Meade, T. J. *Chem. Rev.* **2014**, *114*, 4496.
(7) Stasiuk, G. J.; Long, N. J. *Chem. Commun. (Cambridge, U.K.)* **2013**, *49*, 2732.
(8) Bu, X.-H.; Cao, X.-C.; Zhang, W.-Q.; Zhang, R.-H.; Clifford, T. *Transition Met. Chem. (Dordrecht, Neth.)* **1997**, *22*, 513.
(9) Bu, X.-H.; Cao, X.-C.; Chen, W.; Zhang, R.-H.; Thomas, C. *Polyhedron* **1998**, *17*, 289.
(10) Bu, X.-H.; Lu, S.-L.; Zhang, R.-H.; Liu, H.; Zhu, H.-P.; Liu, Q.-T. *Polyhedron* **2000**, *19*, 431.
(11) Bu, X.-H.; Chen, W.; Mu, L.-J.; Zhang, Z.-H.; Zhang, R.-H.; Clifford, T. *Polyhedron* **2000**, *19*, 2095.
(12) Wang, X.; Zhang, X.; Lin, J.; Chen, J.; Xu, Q.; Guo, Z. *Dalton Trans.* **2003**, 2379.
(13) Yang, N.; Tanner, J. A.; Wang, Z.; Huang, J.-D.; Zheng, B.-J.; Zhu, N.; Sun, H. *Chem. Commun. (Cambridge, U.K.)* **2007**, 4413.
(14) Morfin, J.-F.; Tripier, R.; Baccon, M. L.; Handel, H. *Inorg. Chim. Acta* **2009**, *362*, 1781.
(15) Tsukube, H.; Mizutani, Y.; Shinoda, S.; Okazaki, T.; Tadokoro, M.; Hori, K. *Inorg. Chem.* **1999**, *38*, 3506.
(16) Wada, A.; Watanabe, M.; Yamanoi, Y.; Nankawa, T.; Namiki, K.; Yamasaki, M.; Murata, M.; Nishihara, H. *Bull. Chem. Soc. Jpn.* **2007**, *80*, 335.
(17) Wada, A.; Watanabe, M.; Yamanoi, Y.; Nishihara, H. *Chem. Commun. (Cambridge, U.K.)* **2008**, 1671.
(18) Natrajan, L. S.; Khoabane, N. M.; Dadds, B. L.; Muryn, C. A.; Pritchard, R. G.; Heath, S. L.; Kenwright, A. M.; Kuprov, I.; Faulkner, S. *Inorg. Chem.* **2010**, *49*, 7700.
(19) Schiess, R.; Gertsch, J.; Schweizer, W. B.; Altmann, K.-H. *Org. Lett.* **2011**, *13*, 1436.
(20) Seitz, M.; Oliver, A. G.; Raymond, K. N. *J. Am. Chem. Soc.* **2007**, *129*, 11153.
(21) Raymond, K. N.; Wellman, D. L.; Sgarlata, C.; Hill, A. P. *C. R. Chim.* **2010**, *13*, 849.
(22) Aime, S.; Botta, M.; Ermondi, G. *Inorg. Chem.* **1992**, *31*, 4291.
(23) Aime, S.; Botta, M.; Fasano, M.; Marques, M. P. M.; Geraldes, C. F. G. C.; Pubanz, D.; Merbach, A. E. *Inorg. Chem.* **1997**, *36*, 2059.
(24) Woods, M.; Aime, S.; Botta, M.; Howard, J. A. K.; Moloney, J. M.; Navet, M.; Parker, D.; Port, M.; Rousseaux, O. *J. Am. Chem. Soc.* **2000**, *122*, 9781.
(25) Zhang, S.; Kovacs, Z.; Burgess, S.; Aime, S.; Terreno, E.; Sherry, A. D. *Chem.—Eur. J.* **2001**, *7*, 288.
(26) Lima, L. M. P.; Lecointre, A.; Morfin, J.-F.; de Blas, A.; Visvikis, D.; Charbonnière, L. J.; Platas-Iglesias, C.; Tripier, R. *Inorg. Chem.* **2011**, *50*, 12508.
(27) Thompson, M. K.; Lough, A. J.; White, A. J. P.; Williams, D. J.; Kahwa, I. A. *Inorg. Chem.* **2003**, *42*, 4828.
(28) Misaki, H.; Miyake, H.; Shinoda, S.; Tsukube, H. *Inorg. Chem.* **2009**, *48*, 11921.
(29) Aime, S.; Barge, A.; Benetollo, F.; Bombieri, G.; Botta, M.; Uggeri, F. *Inorg. Chem.* **1997**, *36*, 4287.
(30) Morrow, J. R.; Amin, S.; Lake, C. H.; Churchill, M. R. *Inorg. Chem.* **1993**, *32*, 4566.
(31) Aime, S.; Barge, A.; Botta, M.; Fasano, M.; Ayala, J. D.; Bombieri, G. *Inorg. Chim. Acta* **1996**, *246*, 423.
(32) Purgel, M.; Baranyai, Z.; de Blas, A.; Rodríguez-Blas, T.; Bányai, I.; Platas-Iglesias, C.; Tóth, I. *Inorg. Chem.* **2010**, *49*, 4370.
(33) Jacques, V.; Desreux, J. F. *Inorg. Chem.* **1994**, *33*, 4048.
(34) Woods, M.; Kovacs, Z.; Kiraly, R.; Brücher, E.; Zhang, S.; Sherry, A. D. *Inorg. Chem.* **2004**, *43*, 2845.
(35) Desreux, J. F. *Inorg. Chem.* **1980**, *19*, 1319.
(36) Morrow, J. R.; Chin, K. O. A. *Inorg. Chem.* **1993**, *32*, 3357.
(37) Amin, S.; Morrow, J. R.; Lake, C. H.; Churchill, M. R. *Angew. Chem., Int. Ed.* **1994**, *33*, 773.
(38) Forsberg, J. H.; Delaney, R. M.; Zhao, Q.; Harakas, G.; Chandran, R. *Inorg. Chem.* **1995**, *34*, 3705.
(39) Pittet, P.-A.; Früh, D.; Tissières, V.; G. Bünzli, J.-C. *J. Chem. Soc., Dalton Trans.* **1997**, 895.
(40) Mani, F.; Morassi, R.; Stoppioni, P.; Vacca, A. *J. Chem. Soc., Dalton Trans.* **2001**, 2116.
(41) Helm, L.; Merbach, A. E. *Chem. Rev.* **2005**, *105*, 1923.
(42) Cosentino, U.; Villa, A.; Pitea, D.; Moro, G.; Barone, V.; Maiocchi, A. *J. Am. Chem. Soc.* **2002**, *124*, 4901.
(43) Vaira, M. D.; Stoppioni, P. *New J. Chem.* **2002**, *26*, 136.
(44) Regueiro-Figueroa, M.; Esteban-Gómez, D.; de Blas, A.; Rodríguez-Blas, T.; Platas-Iglesias, C. *Eur. J. Inorg. Chem.* **2010**, *2010*, 3586.
(45) Regueiro-Figueroa, M.; Bensenane, B.; Ruscsák, E.; Esteban-Gómez, D.; Charbonnière, L. J.; Tircsó, G.; Tóth, I.; de Blas, A.; Rodríguez-Blas, T.; Platas-Iglesias, C. *Inorg. Chem.* **2011**, *50*, 4125.
(46) Marenich, A. V.; Cramer, C. J.; Truhlar, D. G. *J. Phys. Chem. B* **2009**, *113*, 6378.
(47) Platas-Iglesias, C. *Eur. J. Inorg. Chem.* **2012**, *2012*, 2023.
(48) Fulmer, G. R.; Miller, A. J. M.; Sherden, N. H.; Gottlieb, H. E.; Nudelman, A.; Stoltz, B. M.; Bercaw, J. E.; Goldberg, K. I. *Organometallics* **2010**, *29*, 2176.
(49) Ammann, C.; Meier, P.; Merbach, A. E. *J. Magn. Reson. (1969—1992)* **1982**, *46*, 319.
(50) *APEX2*, version 2008—4.0; Bruker AXS, Inc.: Madison, WI, 2008.
(51) *SADABS*, version 2012/1; Bruker AXS, Inc.: Madison, WI, 2012.
(52) Sheldrick, G. M. *SHELXTL-97*, version 6.14; University of Göttingen: Göttingen, Germany, 2000.
(53) Sheldrick, G. M. *Acta Crystallogr., Sect. A* **2008**, *64*, 112.
(54) Frisch, M. J.; Trucks, G. W.; Schlegel, H. B.; Scuseria, G. E.; Robb, M. A.; Cheeseman, J. R.; Scalmani, G.; Barone, V.; Mennucci, B.; Petersson, G. A.; Nakatsuji, H.; Caricato, M.; Li, X.; Hratchian, H. P.; Izmaylov, A. F.; Bloino, J.; Zheng, G.; Sonnenberg, J. L.; Hada, M.; Ehara, M.; Toyota, K.; Fukuda, R.; Hasegawa, J.; Ishida, M.; Nakajima, T.; Honda, Y.; Kitao, O.; Nakai, H.; Vreven, T.; Montgomery, J. A., Jr.; Peralta, J. E.; Ogliaro, F.; Bearpark, M.; Heyd, J. J.; Brothers, E.; Kudin, K. N.; Staroverov, V. N.; Keith, T.; Kobayashi, R.; Normand, J.; Raghavachari, K.; Rendell, A.; Burant, J. C.; Iyengar, S. S.; Tomasi, J.; Cossi, M.; Rega, N.; Millam, J. M.; Klene, M.; Knox, J. E.; Cross, J. B.; Bakken, V.; Adamo, C.; Jaramillo, J.; Gomperts, R.; Stratmann, R. E.; Yazyev, O.; Austin, A. J.; Cammi, R.; Pomelli, C.; Ochterski, J. W.; Martin, R. L.; Morokuma, K.; Zakrzewski, V. G.; Voth, G. A.; Salvador, P.; Dannenberg, J. J.; Dapprich, S.; Daniels, A. D.; Farkas, Ö.; Foresman, J. B.; Ortiz, J. V.; Cioslowski, J.; Fox, D. J. *Gaussian 09*, revision B.01; Gaussian, Inc.: Wallingford, CT, 2010.
(55) Lee, C.; Yang, W.; Parr, R. G. *Phys. Rev. B* **1988**, *37*, 785.
(56) Becke, A. D. *J. Chem. Phys.* **1993**, *98*, 5648.
(57) Hehre, W. J.; Ditchfield, R.; Pople, J. A. *J. Chem. Phys.* **1972**, *56*, 2257.
(58) Hariharan, P. C.; Pople, J. A. *Theor. Chim. Acta* **1973**, *28*, 213.
(59) Cao, X.; Dolg, M. *J. Chem. Phys.* **2001**, *115*, 7348.
(60) Cao, X.; Dolg, M. *J. Mol. Struct.: THEOCHEM* **2002**, *581*, 139.
(61) Peng, C.; Schlegel, H. B. *Isr. J. Chem.* **1993**, *33*, 449.
(62) Peng, C.; Ayala, P. Y.; Schlegel, H. B.; Frisch, M. J. *J. Comput. Chem.* **1996**, *17*, 49.
(63) Martin, R. L.; Hay, P. J.; Pratt, L. R. *J. Phys. Chem. A* **1998**, *102*, 3565.